RESEARCH PAPER

Multifunctional nanosheets based on hyaluronic acid modified graphene oxide for tumor-targeting chemo-photothermal therapy

Lin Hou · Qianhua Feng · Yating Wang · Huijuan Zhang ·
Guixiang Jiang · Xiaomin Yang · Junxiao Ren · Xiali Zhu ·
Yuyang Shi · Zhenzhong Zhang

Abstract Graphene oxide (GO) with strong optical absorption in the near-infrared (NIR) region has shown great potential both in photothermal therapy and drug delivery. In this work, hyaluronic acid (HA)-functionalized GO (HA-GO) was successfully synthesized and controlled loading of mitoxantrone (MIT) onto HA-GO via π–π stacking interaction was investigated. The results revealed that drug-loaded nanosheets with high loading efficiency of 45 wt% exhibited pH-sensitive responses to tumor environment. Owing to the receptor-mediated endocytosis, cellular uptake analysis of HA-GO showed enhanced internalization. In vivo optical imaging test demonstrated that HA-GO nanosheets could enhance the targeting ability and residence time in tumor site. Moreover, the anti-tumor activity of free MIT, MIT/GO, and MIT/HA-GO in combination with NIR laser was investigated using human MCF-7 cells. In vitro cytotoxicity study revealed that HA-GO could stand as a biocompatible nanocarrier and MIT/HA-GO demonstrated remarkably higher toxicity than free MIT and MIT/GO, with IC_{50} of 0.79 μg ml^{-1}. Tumor cell-killing potency was enhanced when MIT/HA-GO were combined with NIR irradiation, and the IC_{50} of MIT/HA-GO plus laser irradiation was 0.38 μg ml^{-1}. In vivo, MIT/HA-GO plus NIR laser irradiation with the tumor growth inhibition of 93.52 % displayed greater anti-tumor effect compared with free MIT and MIT/GO with or without laser irradiation. Therefore, the MIT/HA-GO nanosheets may potentially be useful for further development of synergistic cancer therapy.

Lin Hou and Qianhua Feng have contributed equally to this work.

L. Hou · Q. Feng · Y. Wang · H. Zhang ·
G. Jiang · X. Yang · J. Ren · X. Zhu · Y. Shi ·
Z. Zhang (✉)
School of Pharmaceutical Sciences, Zhengzhou
University, 100 Science Road, Zhengzhou 450001, China
e-mail: zhangzz_pharm@163.com

Introduction

Photothermal therapy (PTT), which uses near-infrared (NIR) laser light-generated heat to destroy tumor cells, is an increasingly recognized alternative to treat various cancers in clinic practice. Compared with traditional therapeutic modalities, PTT shows minimal invasive nature and improved selectivity since only the lesion that is exposed to the light is treated, while other tissues without laser irradiation are not affected (Huang et al. 2011; Tian et al. 2011). In recent years, various materials under investigation with high optical

absorbance in the NIR region such as gold nanostructures (Melancon et al. 2011a, b), silver nanoparticles (Boca et al. 2011), and carbon nanotubes (CNTs) (Liu et al. 2011b) have been developed as photothermal conducting agents for PTT treatment of cancer. Nevertheless, these phototherapeutics agents deliver only heat to the tumorigenic region without any drugs. Based on the attractive photothermal property of these nanomaterials to optimize cancer therapy, the combination of hyperthermia with chemotherapeutic agents is an encouraging approach, which can result in synergistic effects that are greater than the two individual treatments alone (Liu et al. 2011a).

Despite the promising application of systems as above in cancer chemo-photothermal therapy, gold and silver nanomaterials have rather low drug loading capacity (Zhang et al. 2011). In addition, the cytotoxicity of CNTs is controversial due to the use of CNTs with or without surface functionalization and the residual heavy metals in CNTs (Liang et al. 2010).

Recently, graphene oxide (GO), as a rising star in materials with two-dimensional structure consisting of sp^2-hybridized carbon, has been studied for drug delivery (Sun et al. 2008) and PTT due to their large surface area, unique photothermal properties as well as relatively low cost (Robinson et al. 2011; Yang et al. 2010). As drug carriers, Yang and colleagues found that the weight ratio of the doxorubicin hydrochloride to the GO could reach 200 % (Yang et al. 2008). Moreover, it has been also reported that GO performed significantly better photothermal sensitivity and lower in vitro toxicity than those of CNTs (Zhang et al. 2010b), thus supporting its possible use in PTT. Accordingly, GO was chosen as the drug carrier and photothermal agents in our study to combine these two abilities in one system.

Mitoxantrone (MIT), a synthetic anthracenedione derivative, is a clinically well-established anticancer agent which shows high efficacy in breast cancer, acute leukemia, and non-Hodgkin's lymphoma (An and Morris 2010). We hypothesized that combining PTT with MIT using GO that mediates simultaneous photothermal effect and drug release (chemo-photothermal therapy) would result in enhanced anti-tumor activity and reduced toxicity.

Notably, successful chemo-photothermal therapy depends on the body distribution of the drug delivery system, and only when this system is introduced into tumor cells, enhanced anti-tumor efficacy could be achieved (Liu et al. 2007). However, most researches of GO only relied on the passive targeting effect (the so-called enhanced permeability and retention, EPR effect) to direct nanocarriers at tumor sites, which might decrease the therapeutic efficacy owing to the lack of cell-specific interactions (Liu et al. 2012). Therefore, a more effective drug delivery strategy should be developed to promote the binding and internalization of nanocarrier through their specific interactions with the receptors expressed on the cell surface of interest.

Hyaluronic acid (HA), which plays important roles in biological functions, such as mediating cell proliferation and differentiation (Entwistle et al. 1996), was utilized here. In particular, since HA can specifically bind to various cancer cells that over-express CD44 and RHAMM, many studies have focused on its pharmaceutical applications for the design of tumor-targeting drug delivery vehicles (Choi et al. 2010; He et al. 2009). Besides, HA have multiple functional groups available for chemical modification so that the HA-modified GO with good biocompatibility, physiological stability, and active tumor-targeting ability could be obtained in our strategy.

Herein, we constructed a multifunctional tumor-targeting drug delivery system employing GO as drug carrier plus photothermal agents, HA as targeting ligand, and MIT as a model chemotherapeutic drug for treatment of breast cancer. As shown in Fig. 1, this system (MIT/HA-GO) could deliver both the heat and drug to the tumorigenic region to facilitate the chemo-photothermal treatment. Controlled loading, physico-chemical characteristics, and in vitro drug release profile of this system were investigated in detail. In addition, the cytotoxicity and in vitro cellular uptake of MIT/HA-GO were monitored on MCF cells to assess internalization via receptor-mediated endocytosis. The in vivo biodistribution and tumor-targeting behavior of HA-GO were observed using non-invasive near-infrared (NIR) fluorescence imaging system by tracking Cy7-labeled HA-GO in MCF-7 tumor-bearing nude mice. Finally, the in vivo synergistic anti-tumor activity of MIT/HA-GO was also evaluated.

Methods and materials

Materials

Graphene oxide was purchased from Nanjing JCNANO Tech Co., Ltd. Sodium hyaluronic acid

Fig. 1 Schematic illustration of the formation, accumulation at tumor site, and synergistic effect of this system. (Color figure online)
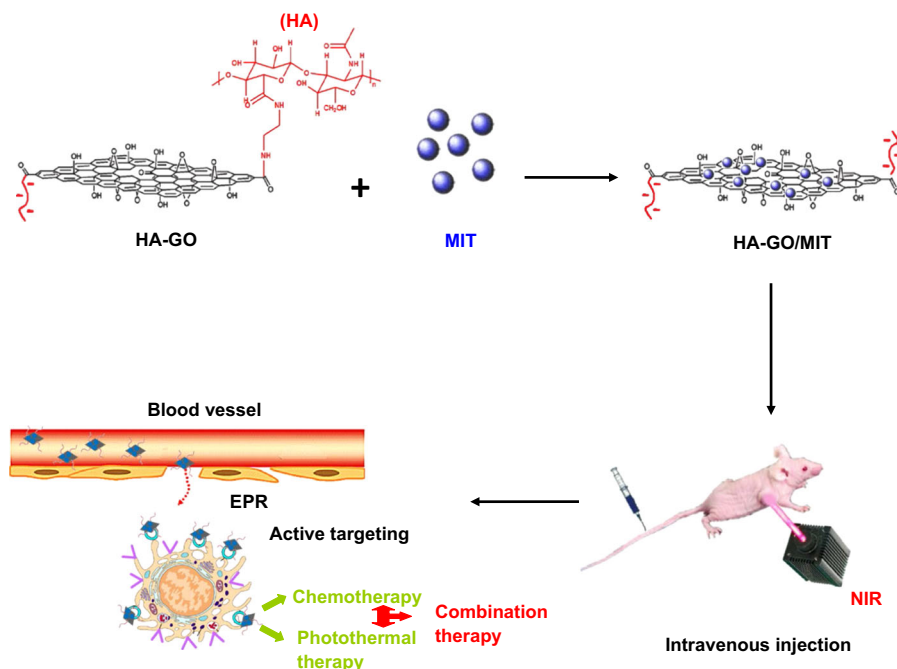
(molecular weights 12 kDa) was obtained from Freda Biochem Co., Ltd. (Shangdong, China). 1-ethyl-3-(3-dimethylaminopropyl) carbodiimide (EDC) (purity of 98.5 %) and *N*-Hydroxysuccinimide (NHS) (purity of 98 %) were bought from Aladdin Reagent Database Inc. (Shanghai, China). Mitoxantrone (MIT) (purity of 99.3 %) was gotten from Beijing YKSD Technology Co., Ltd. All other chemicals were of analytical grade and were used without further purification.

Synthesis and characterization of HA-GO nanosheets

The HA-GO was synthesized by coupling GO with aminated HA [supplementary information (SI) Fig. S1 in ESM] (see SI). The chemical structure and the optical properties of GO and HA-GO were characterized by FTIR and UV/Vis spectroscopy, respectively. The conjugation ratio of HA on GO was determined by UV/Vis measurements based on a standard curve generated with known concentrations of GO in water ($\lambda = 808$ nm) and thermogravimetric analyzer (TGA). In addition, a Kratos Ultra XPS system was used with a monochromatic Al Ka X-ray source operating at 15 kV and 10 mA.

Preparation and characterization of MIT/HA-GO nanosheets

For MIT loading onto HA-GO, 2.5 mg ml^{-1} of HA-GO was first sonicated with MIT (~ 5 mg ml^{-1}) at pH 9 for 0.5 h and then stirred overnight at room temperature. The resulting complexes were centrifuged at 12,000 rpm for 15 min, removed the supernatant, and resuspended by pluronic F 68 plus phospholipid (1:2, w/w) solution. Finally, the solution was dialyzed against an excess amount of distilled water with a dialysis bag (MWCO 3500).

The drug loading (DL) of MIT was calculated by the following equation (see SI):

$$DL\,(\%)$$
$$= \frac{\text{Weight of MIT in nanosheets}}{\text{Weight of MIT in nanosheets} + \text{weight of HA-GO fed initially}}$$
$$\times 100$$

The resultant products of MIT/HA-GO were characterized by UV–Vis spectrophotometer and FTIR spectrometer. The morphology and size distribution were observed by TEM which was operated at an accelerating voltage of 200 ekV.

In vitro release of MIT from nanosheets

To investigate the release behavior of MIT from nanosheets, the MIT/HA-GO sample and free MIT solution as control were placed inside a dialysis bag (MWCO of 12 kDa), which were dialyzed in 100 ml phosphate-buffered saline (PBS) at pH 7.4, 5.8 and 4.5, respectively. The drug release was assumed to start as soon as the dialysis chambers were placed into the reservoir. The release reservoir was kept under constant stirring, and the release samples (1 ml) were taken at predetermined time intervals. The concentration of MIT released from the samples was quantified using HPLC.

Laser irradiation and temperature measurement study

HA-GO and GO suspensions were diluted to a desired concentration (containing 25, 50 or 100 μg ml^{-1} of GO) in PBS. The suspensions were illuminated with an 808-nm continuous-wave NIR laser with the power density of 2 W cm^{-2} and a spot size of 6 $\times$ 8 mm (exposure time 0–6 min). The temperature was measured by an infrared thermometer.

Cellular uptake and internalization

Cellular uptake of nanosheets in MCF-7 cells was visualized and quantified by fluorescent microscope and flow cytometry, respectively. For investigation, fluorescence probe FITC with structure of aromatic nucleus was encapsulated in HA-GO and GO through strong π–π stacking and van der Waals interaction, by mixing FITC solution with HA-GO and GO for 12 h at room temperature.

For fluorescent microscope studies, MCF-7 cells were seeded on culture slides at a density of 5.0 $\times$ 10^5 cells per well (surface area of 1.7 cm^2 per well, four chamber slides) and incubated for 24 h at 37 °C. FITC, alone or entrapped in the nanosheets, was added and incubated for 1, 2, and 4 h, respectively. After removing the supernatant and washing three times with PBS, cells were fixed by 4 % paraformaldehyde for 20 min. Then, they were washed three times with PBS, mounted in Dako fluorescence mounting medium and observed under fluorescent microscope (Eclipse 80i, Nikon, Japan).

For flow cytometry studies, MCF-7 cells were seeded in a six-well plate at a density of 5.0 $\times$ 10^5 per well 24 h prior to study. Cells were then incubated with FITC-loaded nanosheets at 37 °C for designated time period (1, 2 or 4 h). Finally, all the cell samples were washed with PBS for three times, harvested by trypsinization, and collected in PBS to measure the fluorescent intensity. The fluorescent intensity at 430/485 nm of FITC per cell was determined using a FACS-Calibur flow cytometer (BD Biosciences).

In vitro cytotoxicity studies

For in vitro cytotoxicity studies, MCF-7 cells were placed into 96-well plates at 5.0 $\times$ 10^3 cells $well^{-1}$ and allowed to adhere prior to addition of varying concentrations of MIT, MIT/HA-GO, or MIT/GO (containing 0.1, 0.8, 6.4, and 51.2 μg ml^{-1} of MIT). Then the cells were or were not irradiated with an 808-nm continuous-wave NIR laser with the power density of 2 W cm^{-2} for 3 min. After that, the cells were incubated at 37 °C for a further 24, 48, and 72 h. Sulforhodamine B (SRB) assay was used to measure the cell viability at the given time intervals.

In vivo pharmacokinetic study

Free MIT solution, MIT/GO nanosheets or MIT/HA-GO nanosheets were intravenously administered via a tail vein to Sprague–Dawley rats at a dose of 5 mg MIT kg^{-1}. At predetermined times (5, 15, 30 min, 1, 3, 6, 9, and 12 h) after the intravenous (i.v.) injection, blood samples were taken immediately from retro-orbital plexus, and then centrifuged to separate plasma. To prevent oxidative degradation, 5 % ascorbic acid was added to each plasma sample.

The concentrations of MIT in the above samples were determined by HPLC methods as reported (An and Morris 2010) (see SI). The pharmacokinetic parameters were calculated from the average MIT concentrations in the plasma using 3P97.

In vivo imaging analysis

In order to observe the real-time distribution and tumor-targeting ability of HA-GO nanosheets, NIR fluorescent dye, Cyanine 7 (Cy7) was encapsulated into HA-GO and GO nanosheets according to the method for MIT/HA-GO, respectively. Non-invasive optical imaging system was utilized.

Female BALB/C nude mice were inoculated sub-cutaneously in the right armpits with 0.1 ml MCF-7 cell suspension (2.0×10^6). Once the tumor reached approximately 150–200 mm^3 in volume, the mice received an intravenous injection, via the tail vein, of Cy7, Cy7/HA-GO, or Cy7/GO at a dose of 50 μg kg^{-1}. NIRF imaging experiments were performed at 0.5, 1, 3, 5, 7, 12, and 24 h post-injection using a Kodak in vivo imaging system FX PRO (Kodak, USA) equipped with an excitation bandpass filter at 730 nm and an emission at 790 nm. Images were analyzed using the Kodak Molecular Imaging Software 5.x.

To analyze the body distribution, mice were sacrificed at 24 h post-injection and NIR fluorescence images of the excised tumors and major organs such as heart, liver, spleen, lung, and kidney were measured.

In vivo anti-tumor efficacy studies

In vivo anti-tumor efficacy of MIT/HA-GO nanosheets alone or combination with the laser irradiation treatment was assessed by measuring daily tumor volume with a sliding caliper using MCF7-bearing mice. When tumors grew to approximately 150–200 mm^3, mice were randomly divided into six groups receiving different injections as follows: saline, free MIT, GO, HA-GO, MIT/GO, and MIT/HA-GO at the dose of 4 mg MIT kg^{-1} every 2 days for 7 days.

The tumor volume calculation was performed using formula $0.5 \times (a \times b^2)$, where a is the largest and b is the smallest diameter. The inhibition ratio (IR) was used as another index of anti-tumor activity of the formulation tested. At the end of the experiment, the animals were sacrificed and the tumors were weighed. IR was defined as follows:

$$\text{Inhibition ratio } (\%) = ((W_c - W_t)/W_c) \times 100\,\%$$

W_c and W_t stand for the average tumor weight for control group and treatment group, respectively.

For the laser group, the treatment was the same as described above with the exception that 808 nm laser was performed toward the tumor site of tumor-bearing mice for 1 min after administration.

To further evaluate the anti-tumor effect of the formulation as above on the animals, the tumors were excised for pathology.

Statistical analysis

All the data were presented as mean ± SD from three to ten independent measurements in separate independent experiments and analyzed using descriptive statistic and single-factor analysis of variance.

Results and discussion

Synthesis and characterization of HA-GO nanosheets

In the UV/Vis spectra (Fig. 2a), GO showed a broad peak at 227 nm and HA absorbed strongly at 200 nm. After the formation of HA-GO, the absorption redshifted from 227 to 260 nm while the characteristic peak of HA maintained, suggesting that the reaction occurred between HA and GO, and the electronic conjugation within GO nanosheets was restored after the reaction (Shan et al. 2009). Successful conjugation of GO with HA was also confirmed by FTIR spectroscopy, which showed the characteristic peaks of both HA and GO (Fig. 2c). The appearance of the vibration band around 1650 cm^{-1} and the disappearance of the carboxylic group bands at 1733 cm^{-1} substantiated the formation of amide linkages.

In addition, although GO was soluble in water, it tented to aggregate in physiological solutions that were rich in salts or proteins, such as cell medium and serum, whereas HA-GO exhibited an excellent stability in those solutions. This result implied that with attachment of HA, the nanocomposite dissolubility was highly improved, which maintained long-term stability in physiological environment that contained various proteins, organic molecules as well as high salt concentration. Therefore, the HA-GO possesses a good biocompatibility and stability that can act as ideal carriers for potential biological applications.

As HA and GO have been widely investigated as a targeting moiety and photothermal material in cancer drug delivery, respectively, it is necessary to determine their contents in the HA-GO. The amount of conjugated GO in HA-GO was analyzed by measuring the UV/Vis absorbance at 808 nm, and the estimated conjugation ratios of HA to GO were found to be 60 % at the designated feed mole ratio of HA to GO. Serving as an alternative method, the TGA data for HA-GO showed a 71 % weight loss in a nitrogen atmosphere at
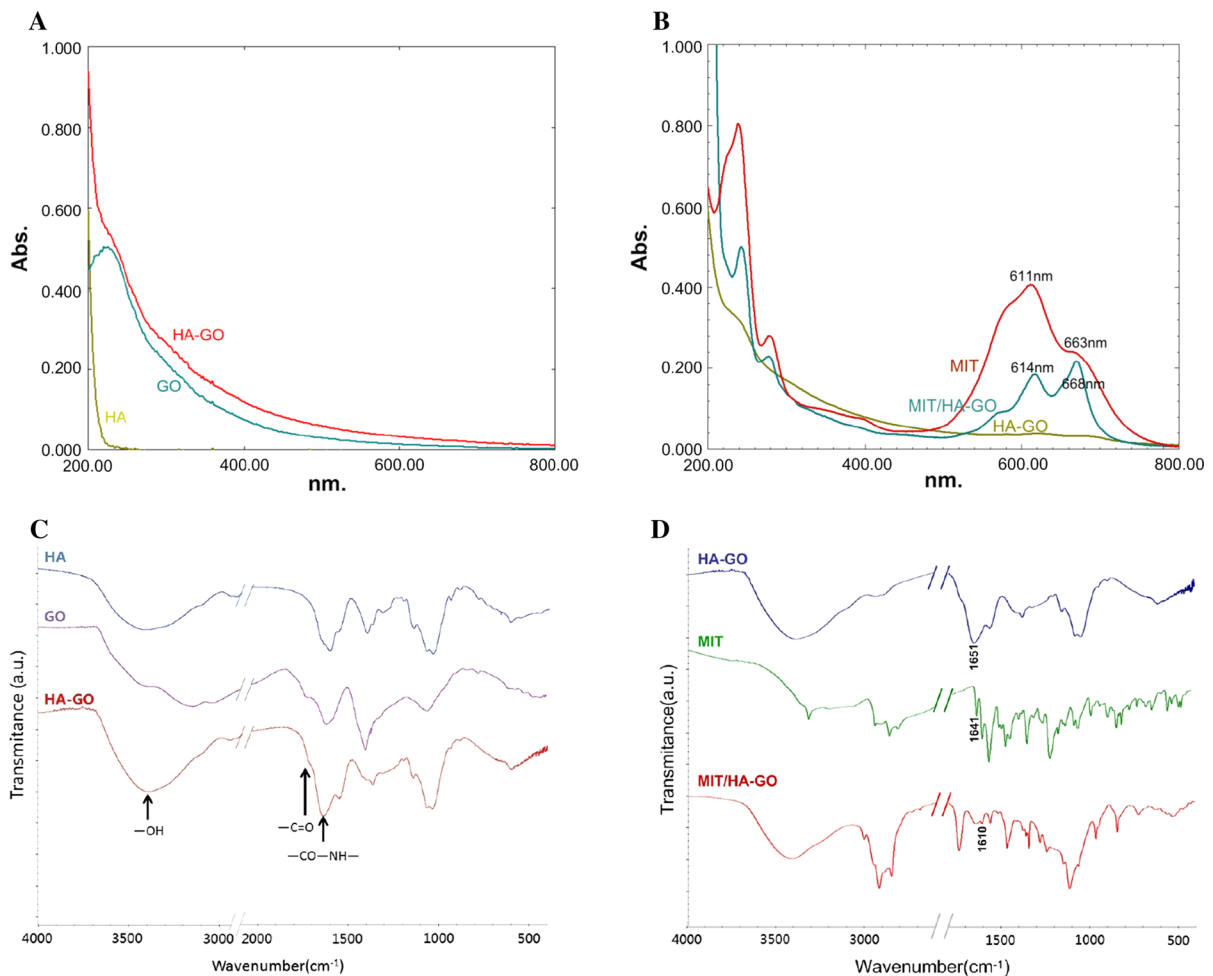
Fig. 2 Characterization of the nanoscaled system: **a** UV/Vis spectra of HA, GO, and HA-GO, **b** UV/Vis spectra of MIT, HA-GO, and MIT/HA-GO, **c** FTIR spectra of the HA, GO, and HA-GO, **d** FTIR spectra of the MIT, HA-GO, and MIT/HA-GO. (Color figure online)

600 °C, whereas GO and pure HA–NH$_2$ had weight losses of 30 % and 100 %, respectively. Compared with the XPS scan spectrum of GO, there is a new peak at ca. 386 eV corresponding to the N 1s binding energy from HA–NH2 chains. From the C 1s XPS spectrum of HA-GO, the C 1s band can be fitted to several components, corresponding to carbon atoms in different positions. As a result, the composite contained about 42 % GO and 58 % HA–NH$_2$.

Preparation and characterization of MIT/HA-GO nanosheets

On the basis of a recent study, GO consists of intact graphitic regions interspersed with sp^3-hybridized

carbons containing carboxyl, hydroxyl, and epoxide functional groups on the edge, top, and bottom surfaces of each sheet and sp^2-hybridized carbons on the aromatic network (Zhu et al. 2010). The large π-conjugated structure of GO can form π–π stacking interaction with the quinone portion of MIT as well as the hydrophobic effect between them. Therefore, MIT noncovalently loaded on GO simply by mixing them in aqueous solution with the aid of slight sonication.

Successful MIT loading on HA-GO was evidenced by the deep blue appearance of the MIT/HA-GO suspension and further confirmed by the UV/Vis spectra (Fig. 2b), in which the characteristic MIT and HA-GO absorption peaks with some changes (red-shift) were clearly identified. It could be seen that the peaks of MIT at 611 and 663 nm shifted to 614 and

668 nm after hybridized with HA-GO, which were generally believed due to the interaction between MIT and HA-GO.

More convincing evidence came from FTIR spectrometer (Fig. 2d). The peak at 1651 cm^{-1} corresponding to v (C=O) in the spectrum of HA-GO and the C=O peak (1641 cm^{-1}) for MIT shifted to a lower position at 1610 cm^{-1} after forming MIT/HA-GO nanohybrid.

The loading capacity of MIT on HA-GO was investigated in different initial MIT concentrations with respect to the fixed concentration of GO ($\sim$5 mg ml^{-1}). It was found that with the increase of the initial MIT concentration, the DL increased and reached the maximum of 45 % at the MIT concentration of 2.5 mg ml^{-1}. This kind of binding was physisorption, mainly via π–π stacking as stated previously by others (Zhang et al. 2010a), while hydroxyl (–OH) groups of MIT could also form a strong hydrogen-bonding interaction with –OH and carboxyl (–COOH) groups in HA-GO. The high DL indicated that HA-GO was a promising carrier for drug delivery.

The morphology of GO, HA-GO, and HA-GO before and after loading with MIT was characterized with TEM, as shown in Fig. 3. The GO remained as micrometer-sized platelets, while the functionalized GO sheets (HA-GO) had sizes in the range of hundreds of nanometers due to the sonication treatment during the synthesis. In addition, GO and HA-GO showed a smooth surface and sharp edges, while many surface protuberances were observed on the surface of MIT/HA-GO nanohybird and the sheet thickness increased. It implied that amount of MIT was immobilized onto the HA-GO sheet. Furthermore, the size of MIT/HA-GO was smaller than that of HA-GO, because π–π stacking and hydrogen

bonding between HA-GO and MIT could induce the nanosheets more compact.

In vitro release of MIT from nanosheets

As shown in Fig. 4, MIT released fairly rapidly in MIT solution and amount of MIT release (%) for this group were 67.35, 79.20, and 86.42 % after 8 h at pH 7.4, 5.8, and 4.5. By contrast, a sustained drug release pattern was observed in the MIT/HA-GO sample. For example, the amount of MIT released for 8 h from the MIT/HA-GO nanosheets was found to be 9.75, 12.88, and 14.85 % at the same condition as above, respectively. This result could be attributed to the interaction between MIT and HA-GO, which delayed drug diffusion and dissolution.

Moreover, it was obvious from Fig. 4 that MIT release from MIT/HA-GO was influenced by pH value, indicating a pH-dependent drug release profile. At pH 7.4, the release amount of MIT was low with less than 15 % within 24 h, while an increased release amount was observed at pH 5.8 and 4.5 with more than 19 % and 25 %, respectively. It was mainly ascribed to the hydrogen-bonding interaction between MIT and HA-GO, which was more prominent in the neutral conditions. However, under acidic conditions, the –OH and –NH– groups of MIT could get protonated leading to the partial dissociation of hydrogen-bonding interaction, and hence the amount of released MIT from HA-GO was higher. On the other hand, MIT became more hydrophilic and water-soluble at low pH, thus resulting in the more release into aqueous environment. These results were similar with earlier report with doxorubicin and single-walled carbon nanotubes (Meng et al. 2012).

This pH-dependent drug release mechanism was important in controlled drug delivery applications,
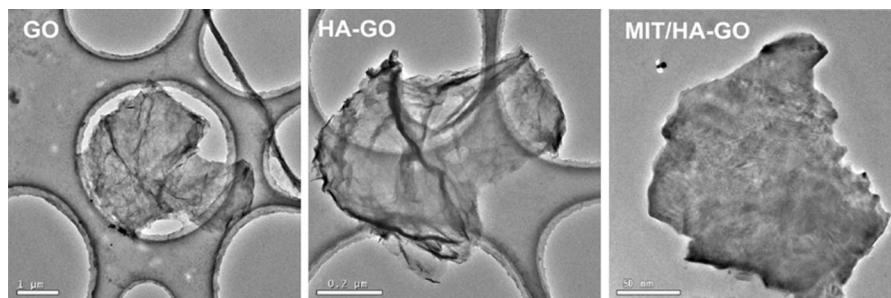

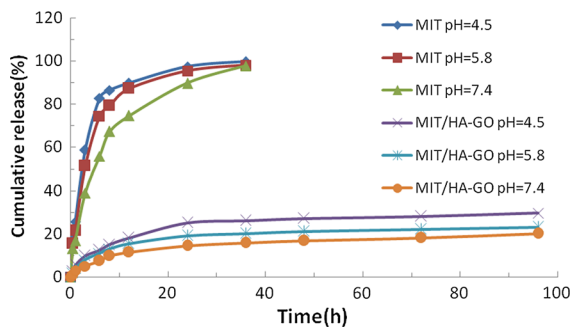**Fig. 3** TEM image of GO, HA-GO, and MIT/HA-GO

Fig. 4 Release profiles of MIT from MIT/HA-GO and free MIT solution at pH 4.5, 5.8, and 7.4. (Color figure online)

Fig. 5 NIR-induced heat generation for PBS suspensions containing various concentrations of GO and HA-GO. (Color figure online)

since both the microenviroments in the extracellular tissues of tumors and intracellular lysosomes as well as endosomes were acidic (Gillies and Frechet 2005; Qin et al. 2013).

Laser irradiation and temperature measurement study

As shown in Fig. 5, both suspensions demonstrated a concentration-dependent and time-dependent temperature increase in response to NIR irradiation. In addition, the heat-generating capacity of HA-GO ($\Delta T \approx 20$ °C at 50 µg ml^{-1} of GO, 6 min) and GO ($\Delta T \approx 19$ °C at 50 µg ml^{-1} of GO, 6 min) was similar, indicating that preparation method did not influence the photothermal sensitivity of GO. This suggested that HA-GO could be served as an effective photothermal agent in cancer treatment.

Cellular uptake and internalization

Internalization of the HA-GO and GO was examined to demonstrate the penetration of nanosheets into the cells and the targeting effects of nanosheets conjugated with HA. In Fig. 6a, the fluorescent signals could be observed when MCF-7 cells incubated with HA-GO and GO for 1 h, while the FITC group showed no obvious signals in cells throughout the studied period. Furthermore, the nanosheets uptake by MCF-7 cells displayed a time-dependent endocytic process. On the other hand, the fluorescence intensity of FITC-labeled HA-GO was stronger than that of FITC-labeled GO, implying higher intracellular uptake capabilities of HA-GO. This finding indicated that FITC-labeled HA-GO could bind to CD44 receptors expressed on
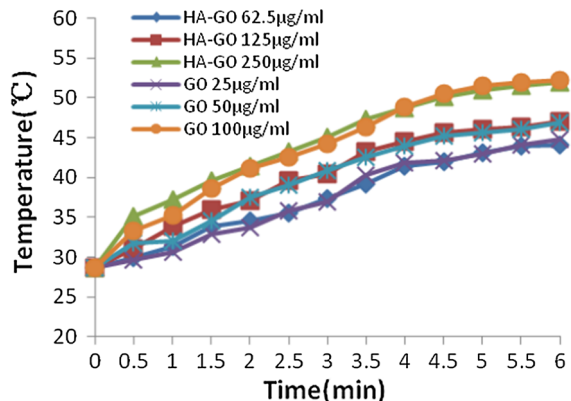
MCF-7 cells (Upadhyay et al. 2010), followed by internalization via receptor-mediated endocytosis. More importantly, the ability of HA to bind its CD44 receptor was not affected by the covalent amide bond, and the receptor-mediated endocytosis was unhindered.

In addition, quantitative analysis of cellular uptake for HA-GO and GO was shown in Fig. 6b. Fluorescence signals were detected when MCF-7 cells incubated with the HA-GO and GO for 1, 2, and 4 h, and the signals become stronger as the time increased. It could be seen that the mean fluorescence intensity for the HA-GO approximately reached 1.34-, 1.72-, and 2.86-fold of that for GO after 1, 2, and 4 h of incubation, respectively.

Therefore, HA-GO with high efficacy of cellular uptake can act as a targeting vehicle for selective delivery of anticancer drugs to tumor cells via specific intracellular signaling pathways.

In vitro cytotoxicity studies

As shown in Fig. 7 about in vitro cytotoxic effects of the drug and formulation, higher drug concentration and longer incubation time would cause lower cell viability, or equivalently higher mortality of the cells. For example, MIT, MIT/GO, and MIT/HA-GO exhibited more than 50 % growth inhibition concentration (IC$_{50}$) of about 5.90, 9.61, and 6.46 µg ml^{-1} at 24 h, and 2.95, 2.2, and 0.79 µg ml^{-1} at 48 h, respectively.

In addition, at the MIT concentration of 0.8 µg ml^{-1} within 24 h, the inhibition rate of free MIT was 28.5 %, indicating a higher cytotoxicity than

MIT/GO (23.1 %) and MIT/HA-GO (27.1 %). The lower cell-killing potency with MIT/GO and MIT/HA-GO could be attributed to relatively stable complexes formed between MIT and GO or HA-GO and delayed MIT release inside cells. However, with the incubation time increased, the MIT/GO and MIT/HA-GO induced a more significant cytotoxic effect on the tumor cells in comparison with free MIT. Furthermore, the percentage of cell growth inhibition increased from ~40 % in the MIT/GO case to ~60 % in the MIT/HA-GO case, which was a significant enhancement. This suggested that MIT/HA-GO could efficiently deliver the drug into the cells owing to the high cellular internalization of HA-modified GO via receptor-binding endocytosis, which was consistent with the results of cellular uptake tests as above.

Figure 7 also demonstrates that there was no obvious toxicity (>80 % cell viability) measured for GO and HA-GO without laser irradiation, revealing that nanocarriers alone were not cytotoxic and the enhanced efficacy should be attributed to the contribution of the drug bound on them.

Finally, the synergetic effect of MIT and HA-GO (a photothermal agent) was accessed under irradiation by NIR laser. Tumor cell-killing potency was enhanced when MIT/HA-GO were combined with NIR irradiation. The inhibition rate of MIT/HA-GO + NIR group at 48 h was significantly increased to 95 % when the MIT concentration was 51.2 $\mu g\ ml^{-1}$, which was higher than that of free MIT and MIT/HA-GO groups (75 and 90 %, respectively). It demonstrated that MIT/HA-GO under laser irradiation could
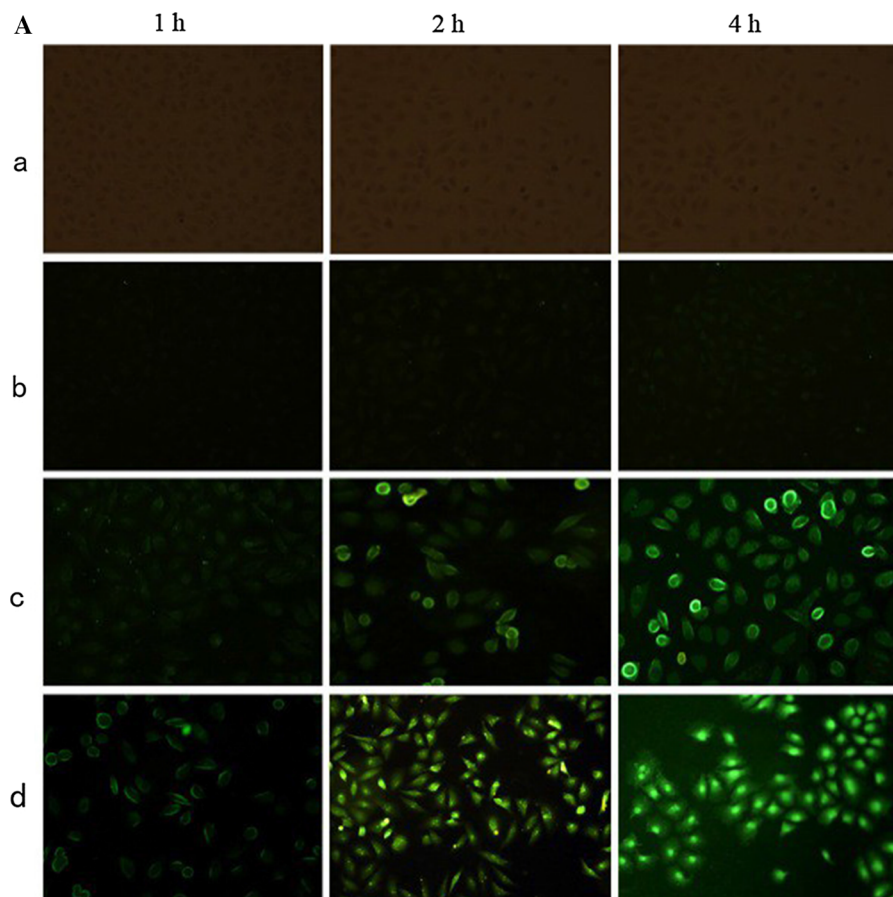

Fig. 6 **a** The internalization images of MCF-7 cells at 1, 2, and 4 h: *a* control group; *b* FITC group; *c* FITC-labeled GO; and *d* FITC-labeled HA-GO. **b** Quantitative cellular uptake of different samples by MCF-7 cells using flow cytometry. (Color figure online)
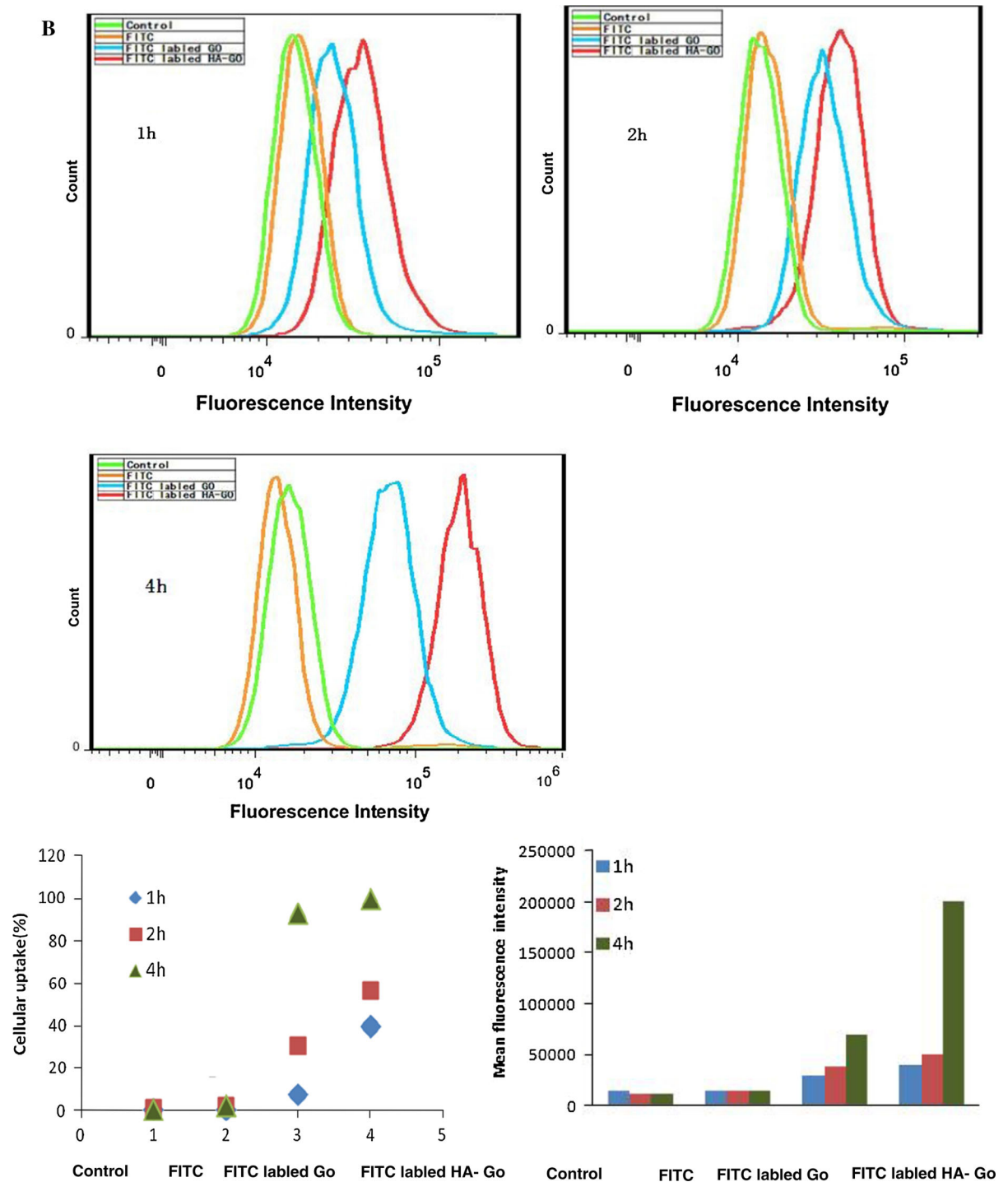
Fig. 6 continued

selectively carry heat and drug to cancer cells and significantly enhance the therapeutic efficacy of chemo-photothermal.

In a word, MIT/HA-GO treated with irradiation displayed the strongest in vitro anti-tumor efficacy because of the combination of chemotherapy with

Fig. 7 Cell viability of MCF-7 cells after treatment with different concentrations of MIT with or without 808-nm laser irradiation. The data represent the means of triplicate measurements. All data are presented as mean ± SD. (Color figure online)
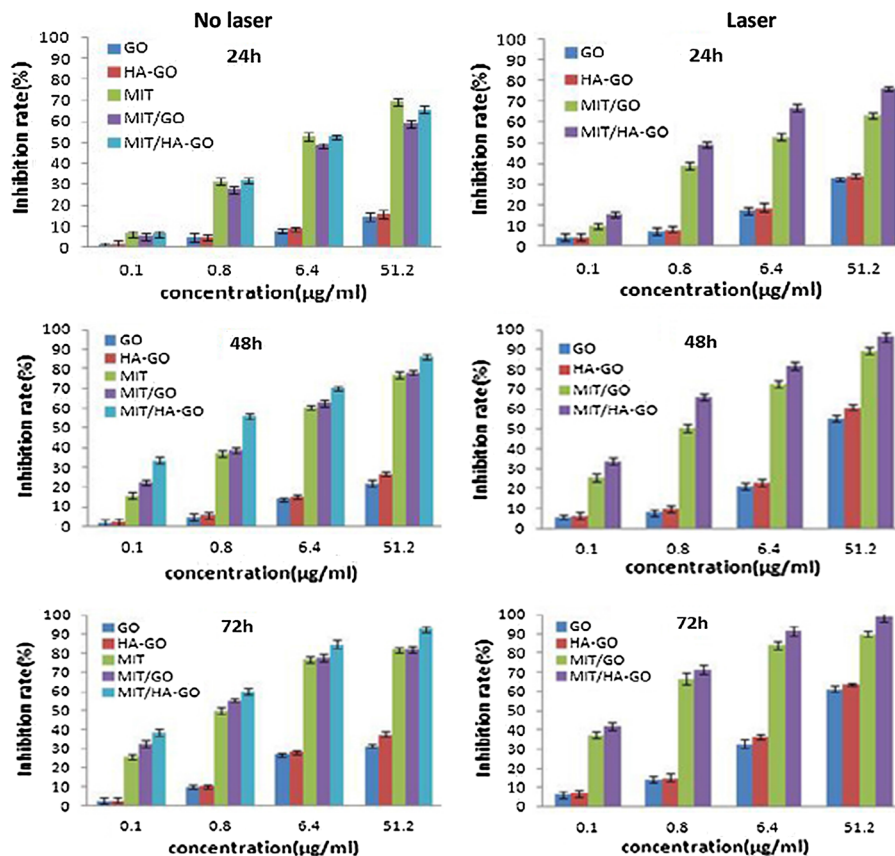
photothermal therapy. It is likely that MIT/HA-GO would be attractive in future anticancer therapy.

In vivo pharmacokinetic study

The plasma concentration–time profiles of MIT after intravenous injection of MIT solution, MIT/HA-GO and MIT/GO nanosheets are shown in Fig. 8, and relevant pharmacokinetic parameters are listed in Table 1. It could be seen that MIT from the solution was cleared rapidly from the blood. On the contrary, MIT/HA-GO and MIT/HO nanosheets exhibited a delayed blood clearance. In addition, MIT level from the nanosheets remained higher at all time points than that of MIT solution. Interestingly, the HA-modified nanosheets achieved a little further prolonged systemic exposure of MIT compared with the MIT/GO, but did not significantly affect the nanosheets' behavior in blood. For example, the MRT were 1.57 and 2.17 h for MIT/GO and MIT/HA-GO, respectively.
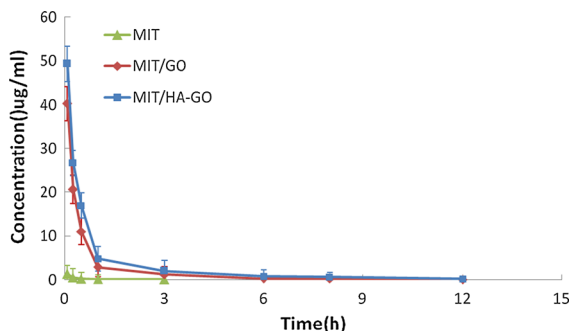

Fig. 8 Plasma concentration–time curves of MIT loaded in MIT solution, MIT/GO, and MIT/HA-GO nanosheets following the i.v. administration of a single dose of 5 mg MIT kg^{-1} in Sprague–Dawley rats. The data represent the mean ± SD, $n = 5$. (Color figure online)

As shown in Table 1, compared with the MIT solution, the MIT/GO and MIT/HA-GO nanosheets provided significantly higher AUC (23.41- and 24.87-fold, respectively), terminal $t_{1/2}$ (1.45- and 1.99-fold, respectively), and MRT (2.71- and 4.45-fold,

respectively) and lower CL (24.58- and 25.94-fold decrease, respectively) of MIT. These in vivo pharmacokinetic properties of MIT from nanosheets were thought to be related to its in vitro sustained MIT release pattern. These results indicated that MIT/HA-GO nanosheets might contribute to the improved therapeutic efficacy.

In vivo imaging analysis

In vivo behavior of HA-GO, the Cy 7-labeled HA-GO, GO, and the free Cy 7 as the control is shown in Fig. 9a. For all the samples, considerable fluorescence signals were detected in the whole body of the mice at the early time points (0.5–1 h), resulting from circulation in the bloodstream, and then gradually decreased as a function of time. For the free Cy 7, the fluorescence signals decreased quickly and became negligible after 12 h. On the other hand, the HA-GO and GO exhibited a strong fluorescence signal for up to 24 h, which was possible due to the prolonged circulation characteristics of the nanosheets.

Interestingly, both HA-GO and GO nanosheets seemed to be excreted via the kidney after injection without much accumulation in other non-target tissue and organs. Although fluorescence signal was

Fig. 9 In vivo non-invasive NIRF images of Cy7-labeled HA-GO, GO, and the free Cy 7 in tumor-bearing mice. **a** Time-dependent whole-body images after intravenous injection. **b** Ex vivo images of major organs harvested from the mice at 24 h post-injection. (Color figure online)

observed in the kidney for 24 h, the fluorescence signal intensity in the kidney was decreased while that in the tumor region was intensified. In particular, compared with the free Cy7, preferential accumulation of fluorescence for Cy7-labeled HA-GO and GO nanosheets was obvious in the tumor site at any time post-injection ranged from 3 to 24 h. Moreover, the HA-GO showed much higher tumor-targeting efficiency than GO which confirmed by enhanced accumulation in tumor. This high tumor targetability of HA-GO might be due to combination of an enhanced permeation and retention (EPR) effect as well as receptor-mediated endocytosis of HA-GO.

After 24 h post-injection, mice were sacrificed, and major organs such as heart, liver, spleen, lung and kidney, as well as the tumors, were isolated to evaluate the in vivo biodistribution behavior. As seen in Fig. 9b, strong fluorescence signals were observed in the tumor issues, and HA-GO presented the stronger fluorescence signal, indicating the tumor-targeting

Table 1 Pharmacokinetic parameters of MIT after i.v. injection of MIT solution, MIT/GO nanosheets, and MIT/HA-GO nanosheets in Sprague–Dawley rats at a dose of 5 mg/kg MIT ($n = 5$)

| Parameter	MIT	GO/MIT	HA-GO/MIT
P (μg ml^{-1})	–	–	62.05 ± 5.86
Gamma (1/h)	–	–	7.60 ± 0.98
A (μg ml^{-1})	2.25 ± 0.20	43.12 ± 3.86	14.36 ± 2.46
α (1/h)	8.74 ± 0.46	3.66 ± 0.30	1.03 ± 0.07
B (μg ml^{-1})	0.35 ± 0.12	3.42 ± 0.38	0.68 ± 0.11
β (1/h)	0.42 ± 0.14	0.30 ± 0.01	0.19 ± 0.06
Vc [(mg kg^{-1})/(μg ml^{-1})]	2.32 ± 0.28	0.09 ± 0.01	0.06 ± 0.01
$t_{1/2(pi)}$ (h)	–	–	0.10 ± 0.01
$t_{1/2(\alpha)}$ (h)	0.08 ± 0.01	0.19 ± 0.02	0.68 ± 0.04
$t_{1/2(\beta)}$ (h)	1.76 ± 0.50	2.33 ± 0.26	4.60 ± 0.54
K_{12} (1/h)	5.19 ± 0.52	1.23 ± 0.05	2.57 ± 0.46
K_{21} (1/h)	1.66 ± 0.45	1.09 ± 0.05	2.97 ± 0.06
K_{13} (1/h)	–	–	0.60 ± 0.08
K_{31} (1/h)	–	–	0.25 ± 0.03
K_{10} (1/h)	2.31 ± 0.89	1.85 ± 0.30	2.44 ± 0.68
CL [mg kg^{-1}h^{-1}/(μg ml^{-1})]	4.67 ± 0.75	0.19 ± 0.05	0.18 ± 0.03
AUC (h μg ml^{-1})	1.25 ± 0.35	29.26 ± 0.47	31.90 ± 0.92
AUMC	1.63 ± 0.69	45.83 ± 3.56	44.36 ± 5.10
MRT (h)	0.47 ± 0.03	1.57 ± 0.04	2.09 ± 0.08
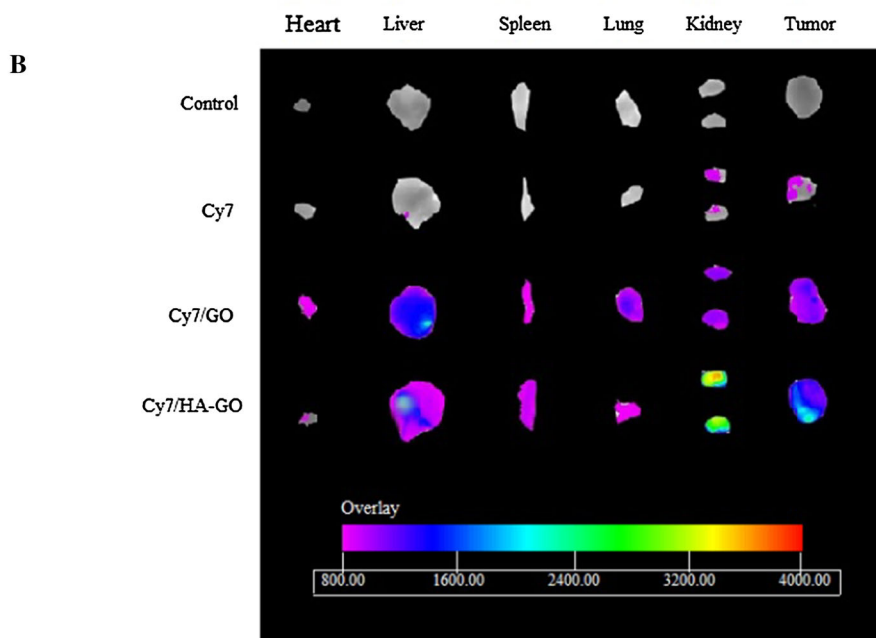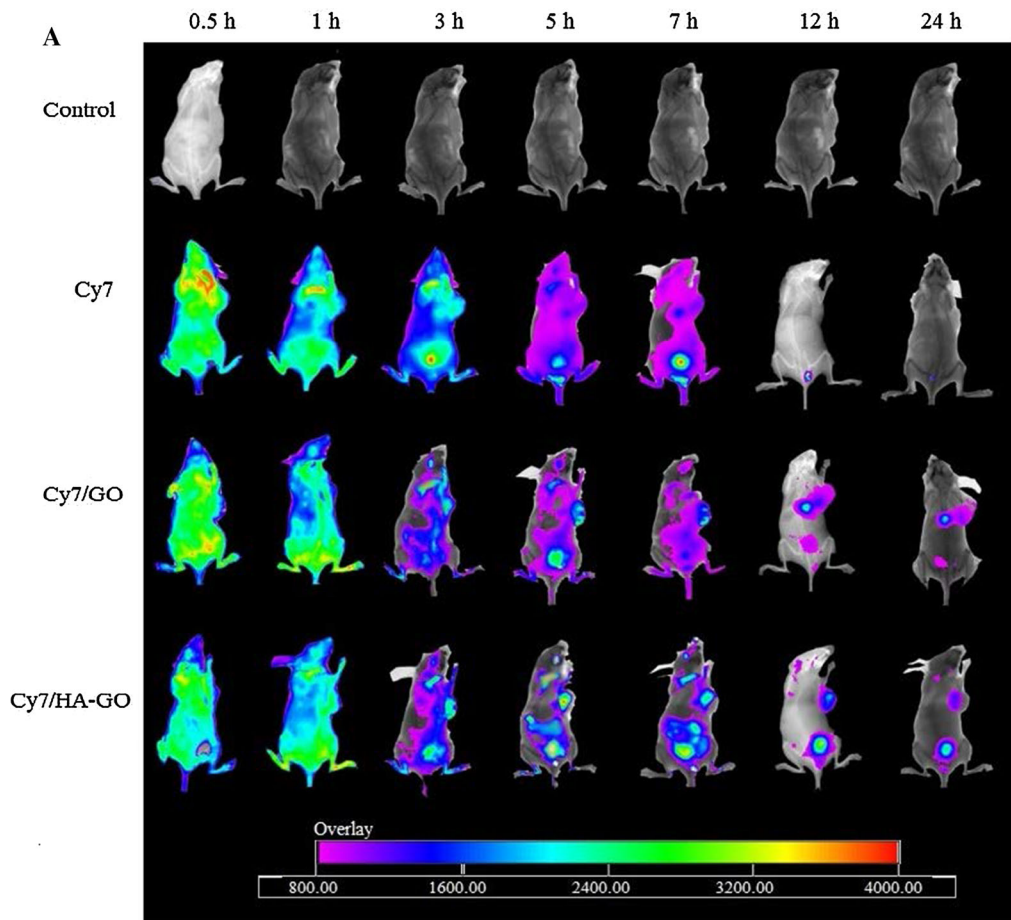
Fig. 10 In vivo anti-tumor
efficacy assay with or
without laser irradiation.
a Relative tumor volumes of
tumor-bearing mice as a
function of time.
b Histological staining of
the excised tumors at 24 h
after injection of *a* saline,
b GO, *c* HA-GO, *d* MIT
solution, *e* MIT/GO, *f* MIT/
HA-GO, *g* MIT + laser,
h MIT/GO + laser, and
i MIT/HA-GO + laser
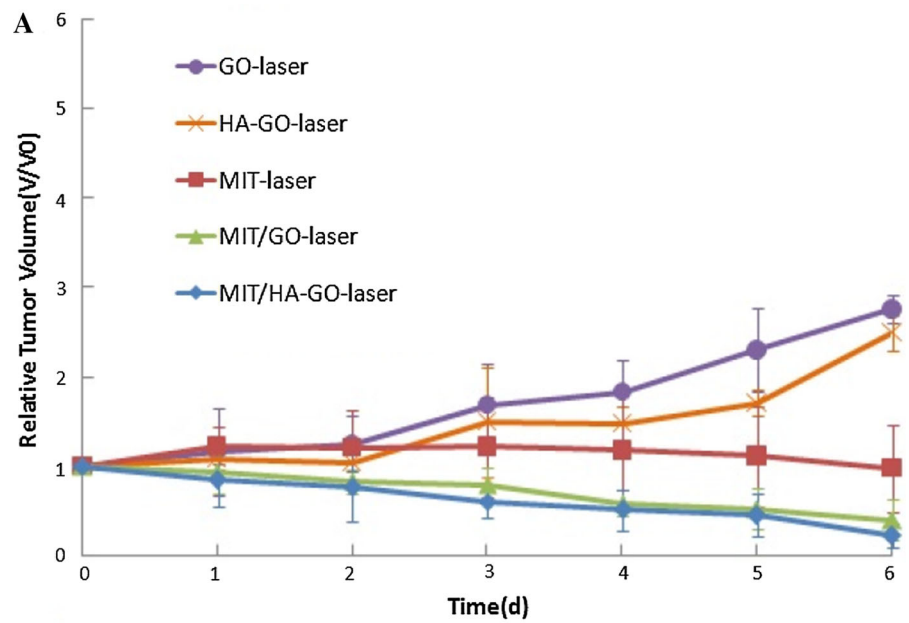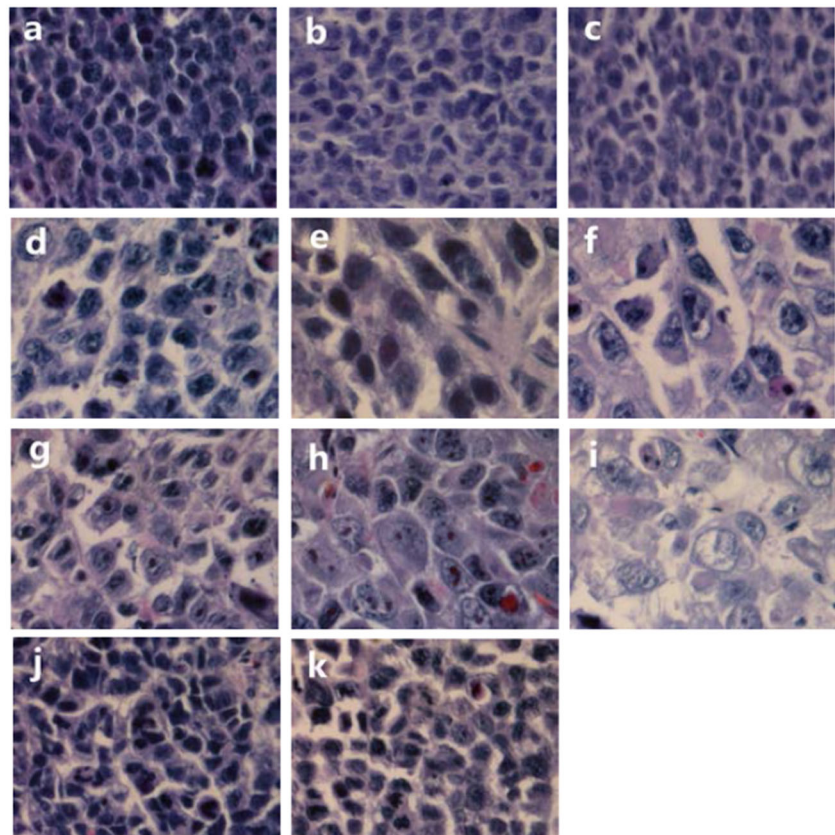
ability of HA-GO. While other tissues showed lower NIRF signals, except for the reticuloendothelial system (RES) organ of liver and kidney, in which the nanosheets were excreted.

These results as above might be determined by several key factors as follows. Firstly, it was reported that long circulation in the blood could be one of the most significant reasons for tumor-targeting efficiency (Hou et al. 2012). HA-GO just displayed prolonged circulation time from our study. Secondly, HA-GO exhibited fast cellular internalization through receptor-mediated endocytosis, which facilitated the tumor-targeting efficacy (Cho et al. 2007).

In vivo anti-tumor efficacy studies

To evaluate the anti-tumor efficacy of MIT/HA-GO, we conducted comparative efficacy studies. The relative tumor volumes after various treatments were monitored for 7 days (Fig. 10a).

Under the condition without irradiation treatment, neither saline nor MIT-free nanosheets (GO and HA-GO) treatments had any substantial effect on the tumor growth, and the tumor volumes increased rapidly. However, free MIT-, MIT/GO-, and MIT/HA-GO-treated mice showed significant anti-tumor therapeutic efficacy, respectively. At 6 day post-injection, the relative tumor volume in free MIT-treated mice was suppressed and reached about 90 %, compared with 328 % attained in saline-treated mice. MIT/GO-treated mice showed more efficient anti-tumor efficacy than free MIT, with the relative tumor volume of 74.85 %. In particular, MIT/HA-GO-treated mice decreased substantially the relative tumor volume by 54.2 %, indicating that MIT/HA-GO could successfully deliver the encapsulated MIT at the target tumor, as previously confirmed by in cell culture system and in vivo imaging data. Moreover, final tumor weight was measured and inhibition ratios were calculated. The results also demonstrated that MIT/HA-GO inhibited tumor growth most efficiently (85.19 %), followed by MIT/GO (74.07 %) and MIT solution (66.67 %), which were consistent with the results from tumor volume measurements.

After laser irradiation, the tumor sizes in all formulations were decreased compared with the control groups without irradiation as above. Nevertheless, tumors in the control group, the irradiation only group (no GO/HA-GO injection) and the GO/

HA-GO only group (no laser irradiation) showed similarly rapid growth, demonstrating that NIR laser irradiation or GO/HA-GO alone did not affect tumor development. By contrast, lower relative tumor volumes were observed in MIT/GO + laser group and MIT/HA-GO + laser group, and GO + laser group as well as HA-GO + laser group also displayed slower tumor growth. Importantly, mice treated with MIT/HA-GO and laser irradiation showed the highest inhibition ratio of 93.52 %, further revealing the excellent efficacy of HA-GO for combined chemotherapy and photothermal therapy of cancer in vivo.

In addition, the observed anti-tumor efficacy as above was evaluated by H and E stating. As shown in Fig. 10b, the groups injected with saline, the irradiation only group, and the GO/HA-GO only group displayed typical pathological characteristic of tumor, such as closely arranged tumor cells. Tumor tissue in the other groups more or less showed spotty necrosis and intercellular blank. In particular, MIT/HA-GO + laser group possessed the most effective tumor-inhibiting ability compared to other groups.

Our finding of significantly enhanced anti-tumor efficacy for MIT/HA-GO + laser versus other groups can be attributed to three reasons: (1) the tumor-targeting and prolonged circulation time of MIT/HA-GO resulted in a higher accumulation in tumor, (2) upon being taken up by tumor tissues, HA-GO served as powerful agent for combined chemotherapy and photothermal therapy of cancer in vivo, which could demonstrated a synergistic effect for the treatment (Adachi et al. 2009; You et al. 2012), and (3) efficient cellular uptake by cancer cells could lead to increased cell-killing effect owing to the cytotoxicity of MIT together with heat-induced protein denaturation and/or DNA or RNA injury (He et al. 2004).

Conclusions

In this work, HA-modified GO was used as a multifunctional nanocarrier to load anticancer drug MIT for chemo-photothermal treatment. HA-GO nanosheets could significantly facilitate specific uptake by cancer cells via receptor-mediated endocytosis and exhibited much higher cytotoxicity. Additionally, MIT/HA-GO showed prolonged circulation time and preferentially accumulation in tumors, which resulted in enhanced therapeutic efficacy. More importantly,

treatment of mice with MIT/HA-GO followed by NIR laser irradiation demonstrated superior anti-tumor efficacy to chemotherapy or photothermal treatment alone. Taken together, the chemo-photothermal strategy mediated through a single nanoconstruct exemplified by MIT/HA-GO represents a promising approach to effective anticancer therapy.

References

Adachi S, Kokura S, Okayama T, Ishikawa T, Takagi T, Handa O, Naito Y, Yoshikawa T (2009) Effect of hyperthermia combined with gemcitabine on apoptotic cell death in cultured human pancreatic cancer cell lines. Int J Hyperth 25:210–219

An G, Morris ME (2010) HPLC analysis of mitoxantrone in mouse plasma and tissues: application in a pharmacokinetic study. J Pharm Biomed Anal 51:750–753

Boca SC, Potara M, Gabudean A-M, Juhem A, Baldeck PL, Astilean S (2011) Chitosan-coated triangular silver nanoparticles as a novel class of biocompatible, highly effective photothermal transducers for in vitro cancer cell therapy. Cancer Lett 311:131–140

Cho YW, Park SA, Han TH, Son DH, Park JS, Oh SJ, Moon DH, Cho KJ, Ahn CH, Byun Y et al (2007) In vivo tumor targeting and radionuclide imaging with self-assembled nanoparticles: mechanisms, key factors, and their implications. Biomaterials 28:1236–1247

Choi KY, Chung H, Min KH, Yoon HY, Kim K, Park JH, Kwon IC, Jeong SY (2010) Self-assembled hyaluronic acid nanoparticles for active tumor targeting. Biomaterials 31:106–114

Entwistle J, Hall CL, Turley EA (1996) HA receptors: regulators of signalling to the cytoskeleton. J Cell Biochem 61:569–577

Gillies ER, Frechet JM (2005) pH-responsive copolymer assemblies for controlled release of doxorubicin. Bioconjug Chem 16:361–368

He X, Wolkers WF, Crowe JH, Swanlund DJ, Bischof JC (2004) In situ thermal denaturation of proteins in dunning AT-1 prostate cancer cells: implication for hyperthermic cell injury. Ann Biomed Eng 32:1384–1398

He M, Zhao Z, Yin L, Tang C, Yin C (2009) Hyaluronic acid coated poly(butyl cyanoacrylate) nanoparticles as anticancer drug carriers. Int J Pharm 373:165–173

Hou L, Yao J, Zhou J, Zhang Q (2012) Pharmacokinetics of a paclitaxel-loaded low molecular weight heparin-all-trans-retinoid acid conjugate ternary nanoparticulate drug delivery system. Biomaterials 33:5431–5440

Huang P, Xu C, Lin J, Wang C, Wang X, Zhang C, Zhou X, Guo S, Cui D (2011) Folic acid-conjugated graphene oxide loaded with photosensitizers for targeting photodynamic therapy. Theranostics 1:240–250

Liang C, Li H, Wang L, Chen X, Zhao W (2010) Investigation of the cytotoxicity of carbon nanotubes using hydroxyapatite as a nano-matrix towards mouse fibroblast cells. Mater Chem Phys 124:21–24

Liu J, Ohta S, Sonoda A, Yamada M, Yamamoto M, Nitta N, Murata K, Tabata Y (2007) Preparation of PEG-conjugated fullerene containing Gd3+ ions for photodynamic therapy. J Control Release 117:104–110

Liu H, Chen D, Li L, Liu T, Tan L, Wu X, Tang F (2011a) Multifunctional gold nanoshells on silica nanorattles: a platform for the combination of photothermal therapy and chemotherapy with low systemic toxicity. Angew Chem Int Ed Engl 50:891–895

Liu X, Tao H, Yang K, Zhang S, Lee S-T, Liu Z (2011b) Optimization of surface chemistry on single-walled carbon nanotubes for in vivo photothermal ablation of tumors. Biomaterials 32:144–151

Liu H, Liu T, Wu X, Li L, Tan L, Chen D, Tang F (2012) Targeting gold nanoshells on silica nanorattles: a drug cocktail to fight breast tumors via a single irradiation with near-infrared laser light. Adv Mater 24:755–761

Melancon MP, Elliott AM, Shetty A, Huang Q, Stafford RJ, Li C (2011a) Near-infrared light modulated photothermal effect increases vascular perfusion and enhances polymeric drug delivery. J Control Release 156:265–272

Melancon MP, Lu W, Zhong M, Zhou M, Liang G, Elliott AM, Hazle JD, Myers JN, Li C, Stafford RJ (2011b) Targeted multifunctional gold-based nanoshells for magnetic resonance-guided laser ablation of head and neck cancer. Biomaterials 32:7600–7608

Meng L, Zhang X, Lu Q, Fei Z, Dyson PJ (2012) Single walled carbon nanotubes as drug delivery vehicles: targeting doxorubicin to tumors. Biomaterials 33:1689–1698

Qin XC, Guo ZY, Liu ZM, Zhang W, Wan MM, Yang BW (2013) Folic acid-conjugated graphene oxide for cancer targeted chemo-photothermal therapy. J Photochem Photobiol B 120:156–162

Robinson JT, Tabakman SM, Liang Y, Wang H, Casalongue HS, Vinh D, Dai H (2011) Ultrasmall reduced graphene oxide with high near-infrared absorbance for photothermal therapy. J Am Chem Soc 133:6825–6831

Shan C, Yang H, Han D, Zhang Q, Ivaska A, Niu L (2009) Water-soluble graphene covalently functionalized by biocompatible poly-L-lysine. Langmuir 25:12030–12033

Sun X, Liu Z, Welsher K, Robinson JT, Goodwin A, Zaric S, Dai H (2008) Nano-graphene oxide for cellular imaging and drug delivery. Nano Res 1:203–212

Tian B, Wang C, Zhang S, Feng L, Liu Z (2011) Photothermally enhanced photodynamic therapy delivered by nano-graphene oxide. ACS Nano 5:7000–7009

Upadhyay KK, Bhatt AN, Mishra AK, Dwarakanath BS, Jain S, Schatz C, Le Meins JF, Farooque A, Chandraiah G, Jain AK et al (2010) The intracellular drug delivery and anti tumor activity of doxorubicin loaded poly(gamma-benzyl L-glutamate)-b-hyaluronan polymersomes. Biomaterials 31:2882–2892

Yang X, Zhang X, Liu Z, Ma Y, Huang Y, Chen Y (2008) High-efficiency loading and controlled release of doxorubicin hydrochloride on graphene oxide. J Phys Chem C 112:17554–17558

Yang K, Zhang S, Zhang G, Sun X, Lee ST, Liu Z (2010) Graphene in mice: ultrahigh in vivo tumor uptake and efficient photothermal therapy. Nano Lett 10:3318–3323

You J, Zhang R, Zhang G, Zhong M, Liu Y, Van Pelt CS, Liang D, Wei W, Sood AK, Li C (2012) Photothermal-chemotherapy with doxorubicin-loaded hollow gold nanospheres: a platform for near-infrared light-trigged drug release. J Control Release 158:319–328

Zhang L, Xia J, Zhao Q, Liu L, Zhang Z (2010a) Functional graphene oxide as a nanocarrier for controlled loading and targeted delivery of mixed anticancer drugs. Small 6:537–544

Zhang Y, Ali SF, Dervishi E, Xu Y, Li Z, Casciano D, Biris AS (2010b) Cytotoxicity effects of graphene and single-wall carbon nanotubes in neural phaeochromocytoma-derived PC12 cells. ACS Nano 4:3181–3186

Zhang W, Guo Z, Huang D, Liu Z, Guo X, Zhong H (2011) Synergistic effect of chemo-photothermal therapy using PEGylated graphene oxide. Biomaterials 32:8555–8561

Zhu Y, Murali S, Cai W, Li X, Suk JW, Potts JR, Ruoff RS (2010) Graphene and graphene oxide: synthesis, properties, and applications. Adv Mater 22:3906–3924